

Enhancing Cloud Detection in Polar Regions Using Combined Spectral and Textural Features for Landsat 8/9 OLI Imagery

Xinran Shen, Teng Li*, Chong Liu, Shaoyin Wang, Lei Zheng, Qi Liang, Xiao Cheng* and Jiaqi Yao

Abstract—Remote sensing is a cost-effective and efficient method for studying polar regions. However, cloud cover in optical remote sensing images can diminish the data integrity for certain snow/ice applications. Existing cloud detection algorithms are primarily designed for mid and low latitude images, which poses significant challenges in polar regions due to the similar spectral characteristics of clouds and snow/ice surface. This study proposes a new cloud detection algorithm for Landsat 8/9 OLI/TIRS images, which combines spectral and texture features to more accurately differentiate clouds from snow. Initially, the algorithm employs Fmask for preliminary cloud detection, followed by a block processing strategy that integrates the gray-level co-occurrence matrix to extract local texture features for secondary discrimination, helping to eliminate snow misidentified as clouds. Additionally, the algorithm utilizes short-wave infrared (1.57–1.65 μm) and cirrus bands (1.36–1.38 μm) to extract cirrus clouds and employs morphological closing operations to fill gaps in the cloud mask. The algorithm maintains an average accuracy of approximately 97% for different types of clouds. Tested on the Landsat 8 Cloud Cover Assessment Validation Data, a cloud mask dataset verified by experts, this algorithm achieves an average detection accuracy of 93%, signifying improvements of 37% and 45% over the ACCA and Fmask algorithms, respectively. Texture-based methods effectively reduce snow-cloud misclassification but may inadvertently misclassify texturally similar features, highlighting the need for improved discrimination in classification algorithms. In summary, this novel method significantly enhances the efficiency and precision of cloud detection in polar optical remote sensing images. Consequently, it improves the accuracy of other quantitative remote sensing investigations, such as atmosphere correction, albedo estimation and so on.

Index Terms—Cloud detection, Fmask, Polar regions, Landsat 8/9, Cloud-snow differentiation

I. INTRODUCTION

Remote sensing plays a crucial role for snow and ice researches in polar regions, such as sea ice area variations [1],

Manuscript received Apr xx, 2025; revised Apr xx, 2025; accepted May xx, 2025. Date of publication xx, 2025; date of current version xx, 2025. This work was supported in part by the National Natural Science Foundation of China (Grant No. 42206249, 42371344, 42306256 and 42422606) the Innovation Group Project of Southern Marine Science and Engineering Guangdong Laboratory (Zhuhai) under Grant (311021008). (*Corresponding authors:* Teng Li, Xiao Cheng.)

X. Shen is with School of Geospatial Engineering and Science, Sun Yat-Sen University, Zhuhai 519082, China; e-mail: shenxr3@mail2.sysu.edu.cn.

T. Li, C. Liu, S. Wang, L. Zheng, Q. Liang, X. Cheng is with School of Geospatial Engineering and Science, Southern Marine Science and Engineering Guangdong Laboratory, Sun Yat-Sen University, Zhuhai 519082, China; e-mail: {liteng28, liuc, wangshy96, zhengle6, liangq57, chengxiao9}@mail.sysu.edu.cn.

Jiaqi Yao is with the Academy of Ecological Civilization Development for JING-JIN-JI megalopolis, Tianjin Normal University, Tianjin 300387, China. email: yaojiaqi@tjnu.edu.cn.

Color versions of one or more of the figures in this article are available online at <http://ieeexplore.ieee.org>.

Digital Object Identifier 88.8888/JSTARS.2024.8888888

iceberg calving and tracking [2], ice flow velocity estimation [3] etc., which are of great significance in monitoring the feedbacks among Earth system, especially the response of climate change in recent decades [4]. Optical satellite imagery is frequently affected by cloud cover, leading to data gaps or reduced quality for some specific applications, diminishing the integrity of optical satellite image analysis [5]. According to the International Satellite Cloud Climatology Project Flux Data (ISCCP-FD) dataset, the global average cloud cover is estimated to be about 66% [6]. Clouds and their shadows are one of the main noise sources in terrestrial optical satellite data, and their detection is a prerequisite and foundation for most quantitative remote sensing analyses [7]–[10]. Feng and Wang analyzed the significance of cloud-free data in hydrological research using cloud-free Landsat 8 imagery [11], indicating that the average annual number of cloud-free observations by the Landsat 8 satellite is 21.8 ± 14.7 times, with fewer cloud-free observation data from the polar region. Given the special climatic conditions in polar regions, cloud-free remote sensing imagery may be even scarcer [12]. Currently, cloud detection in polar regions with optical satellite images is a challenging issue in the field of satellite image recognition.

Now available cloud detection methods can be categorized into three types: traditional methods based on spectral threshold, cloud detection based on machine learning, and cloud detection based on deep learning [13]. Irish et al. introduced the ACCA (Automatic Cloud Cover Assessment) algorithm for Landsat 7 ETM+ [14], which decides the presence of clouds based on their reflective and thermal properties. It achieves good detection accuracy in middle and low latitude regions and used to be a common algorithm in Landsat imagery cloud detection, which laid the foundation for further development of more advanced cloud detection algorithm for Landsat satellites. Zhu et al. further developed the Fmask (Function of mask) algorithm [8] based on ACCA, used for automated clouds, cloud shadows, snow, and water masking for Landsat 4–9 and Sentinel 2 images. Fmask is arguably the most dominantly used cloud detection approach for Landsat series. However, due to the similar spectral characteristics of clouds and snow, these methods still suffer from certain misclassification for bright cold snow/ice and cloud in polar regions [8]. Beyond spectral feature analysis, current cloud detection methodologies also encompass multidimensional frameworks such as spectral characteristics, spectral-spatial interactions, temporal-spectral variations, spatiotemporal-spectral correlations, and multi-source data integration [15], therefore machine learning algorithms demonstrating comprehensive feature integration capabilities have been extensively applied to cloud detection tasks. Cloud detection methods based on machine learning use

artificially selected image features as samples to train machine learning models such as SVM for pixel or image block classification [16], [17]. Machine learning based on spectral features is a common approach to cloud detection [18], thus have similar difficulty for cloud detection in polar regions. Cloud detection, as a specialized branch of remote sensing image processing, is fundamentally a pixel-wise classification task. This characterization is substantiated by the extensive employment of classification algorithms such as Random Forest [19], which have also demonstrated effective applicability in cloud detection tasks [20]. In addition to spectral features, texture features are also introduced for cloud detection [17], [21]. However, due to the limitation of training samples, their generalizability is poor, and model needs to be re-trained when scenes change [22]. Later, with the development of deep learning, more complex models have been widely used in the field of image classification and also applied to cloud detection in remote sensing imagery [23], [24]. Francis et al. proposed the CloudFCN which shows robustness to many different terrains and sensor types [25]. Jeppesen et al. proposed the RS-Net (Remote Sensing Network) model based on the U-net framework [26], achieving high-precision cloud detection using visible channels; in addition, models like CDnetV2 [27] and others have been used for cloud detection and show promising results. Some state-of-the-art methodologies employ self-attention mechanisms to improve global context modeling for cloud-shadow relationships while boosting computational efficiency [28]. Besides, cloud detection based on generative adversarial networks (GANs) performed well in weakly-supervised learning through synthetic pseudo-label generation [29]. However, such algorithms could show reduced accuracy on tenuous and broken clouds [30]. Deep learning requires a large volume of samples, labeling costs, and long computation times, limiting their extension to wider applications, especially in operational scenarios which require high timeliness. In summary, existing cloud detection methods face challenges in polar regions due to spectral similarities between clouds/snow and dependencies on extensive training data or computational resources.

In polar regions, cloud and snow pixels often exhibit similar characteristics in optical remote sensing images, such as high reflectivity and low temperature, which pose challenges to cloud detection tasks [31]. Additionally, since cirrus clouds are primarily composed of ice crystals, their reflection and texture characteristics are more complex [32]. For example, an earlier version of Fmask may also identify other very bright and cold land features as clouds and may neglect the cirrus clouds [8], so Zhu et al. proposed an improved version of Fmask to better extract cirrus [33], and further proposed Fmask4.0 for better distinguishing snow/ice from clouds in polar regions [34]. Fmask4.0 use the local Standard Deviation (SD) of green band and Normalized Difference Snow Index (NDSI) to distinguish homogenous snow/ice from clouds. It can effectively extract most cloud pixels and part of snow pixels will be accurately distinguished from the cloud mask, but not completely due to insufficient exploitation of texture characteristics. Wu and Han's research proposed an algorithm based on fractal summation method and spatial analysis to

extract clouds, achieving a better effect on the images with high brightness reflectivity [35]. Chen et al. proposed using gray-level co-occurrence matrix to extract texture features of the image and then using machine learning models to segment clouds and snow [17], but this algorithm depends on sample quality and lacks robustness. Guo et al. proposed the CDnetV2 algorithm [27], which also achieved high-precision discrimination between clouds and snow, obtaining high detection accuracy in most challenging conditions, but it performs poorly in identifying tenuous clouds and fine-particle clouds. Dong et al. used prior information about reflectance and forward radiative transfer modeling for cloud detection [36]. They utilized the MOD09 surface reflectance product to establish a monthly composite surface reflectance database and 6S model to simulate the correlation between surface reflectance and Top-of-Atmosphere (TOA) reflectance under different conditions. This method requires accurate prior reflectance data, and the detection results are easily influenced by factors such as snow and ice melting. The unique conditions such as low solar elevation angles, similar reflectance and temperature between snow and clouds makes it more difficult for spectral-based cloud detection, reducing performances of many algorithms. However, snow and clouds' textures differ: polar snow is smooth and uniform, while clouds are rough. Some methods tried to employ texture features [16], [17], [21], but they failed to systematically analyze the differences between cloud and snow, and overlook cirrus clouds, limiting their effectiveness for cloud and snow distinction.

To tackle this problem, this paper proposes a cloud detection method based on spectral and texture features, aiming to accurately and quickly detect cloud in polar regions without pre-training. We categorized the clouds into two types: normal clouds and cirrus clouds, and sequentially extracted them based on their differences in spectral features and texture features compared to snow.

This paper is organized as follows. We begin by outlining the study area and providing details about the data used. Next, we present a comprehensive description of our algorithm, which consists of two main components: spectral detection and texture detection, with separate processing for normal clouds and cirrus clouds. To validate the proposed algorithm, we evaluated the results in two steps. First, we selected scenes with varying cloud types to examine the algorithm's robustness and improvements compared to Fmask4.6. We then used a publicly available dataset for further analysis and compared our results with those of existing algorithms. In the discussion section, we examine the influence of cloud definitions on cloud detection accuracy and explore additional factors that may affect the accuracy of our algorithm. Finally, we prospect potential avenues for operational application of the algorithm as well as its future extendibility to other sensors.

II. STUDY AREA AND DATA

A. Introduction to Target Area

This study primarily focuses on the detection of clouds in polar regions, including Antarctica, Greenland ice sheets and surrounding ocean, Tibetan Plateau and Tianshan Mountains.

Clouds are an important regulator of the polar climate. They consist of moisture and produce precipitation, contributing positively to the surface mass balance [37], [38]. Additionally, by reflecting incoming shortwave radiation and trapping terrestrial longwave radiation, clouds have a profound impact on the surface energy balance of the ice sheet surface [39]. Depending on the cloud characteristics, the dominating effect differs [40]. In most climate models, cloud cover is often underestimated [41]. The estimates of cloud cover over Antarctica derived from active remote sensing and passive remote sensing exhibit a discrepancy of approximately 40% [42]. Surface observations indicate that the fractional cloud cover at the South Pole remains relatively stable at approximately 50-60% across all seasons. In contrast, the cloud cover significantly increases to around 80-90% near the coast of the continent [12].

The cloud cover differences among multiple satellite cloud mask products had significant temporal and spatial heterogeneities in Arctic [43]. The largest uncertainties were seen over Greenland, while substantial inconsistency also occurred on the central and Pacific sides of the Arctic Ocean [43].

The distribution of the remote sensing data used in this study are indicated in the red area shown in Fig.1.

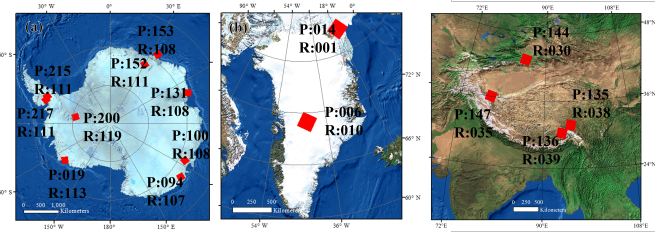


Fig. 1. Spatial distribution of Landsat imagery (Red Rectangle) data utilized in this study with their path and row number labeled. (a) Antarctic, (b) Greenland, (c) Tibetan Plateau.

B. Data Selection

The primary data source employed in this study is the Landsat 8/9 OLI/TIRS Collection 2 Level 1 data. Landsat 8 maintains consistency in spatial resolution and spectral characteristics with its predecessor Landsat satellites, featuring 11 spectral bands. Bands 1-7 and 9-11 have a spatial resolution of 30 m, while Band 8, the panchromatic band, has a resolution of 15 m (See Fig.2). The satellite accomplishes global coverage every 16 days. Landsat 8/9 has added a cirrus band, which aids in the detection of cirrus clouds.

We selected eleven images for the experiment (Table I), comprising nine from Antarctica and two from Greenland. These images contain a variety of cloud types, including tenuous, thick, and cirrus clouds, and represent both inland ice sheet and coastal areas to validate the algorithm's robustness to different polar environments.

This study utilizes the “Landsat 8 Cloud Cover Assessment Validation Data” [44], [45] dataset, formerly known as L8 Biome, for accuracy assessment. This dataset includes 96 pre-collected scenes of Landsat 8 OLI and TIRS Level-1T data, accompanied by manually generated cloud masks

for validating cloud cover assessment algorithms, which includes 12 scenes from the snow-ice regions of Antarctica and Greenland. We use 3 scenes to evaluate the performance of the proposed algorithm. The experimental data for this study can be downloaded from EarthExplorer-USGS (<https://earthexplorer.usgs.gov/>).

Table I: File Names of Landsat 8/9 OLI/TIRS Images Used in This Study

Source of Imagery	File Name
Landsat 8 OLI/TIRS	LC08L1TP014001202307312023080502T1
	LC08L1GT131108202309212023092102RT
	LC08L1GT094107202502112025021102RT
	LC08L1TP136039202404032024041102T1
	LC08L1TP147035202501292025013102T1
Landsat 9 OLI/TIRS	LC09L1GT21511120240131202401302T2
	LC09L1GT153108202403172024031702T2
	LC09L1GT019113202411012024110102T2
	LC09L1GT152111202502092025020902T2
	LC09L1GT100108202502132025021302T2
	LC09L1TP135038202504232025042302T1
Landsat 8 Biome	LC08L1GT200119201312012020101602T2
	LC08L1GT006010201405272020091102T2
	LC08L1GT217111201410242020101602T2

III. METHODOLOGY

The cloud detection technical flowchart is shown in Fig.3. The algorithm comprises two primary components: normal cloud detection, which includes both thick and tenuous clouds, and cirrus cloud detection. Spectral cloud detection based on Fmask are used for primary normal cloud detection, extracting potential cloud pixels firstly. Subsequently, an image segmentation strategy is employed to differentiate between clouds and snow based on their texture feature differences. Additionally, cirrus clouds are separately extracted using the band 9(1.36-1.38 μm) with similar spectral and textural strategy. Finally, morphological operations are used to fill undesired holes.

A. Initial Cloud Detection Based on Fmask

In polar ice and snow environments, cloud detection initially involves distinguishing clouds from other land features such as water bodies, bare rock, and snow. We use Fmask4.6 to detect clouds in the first step. Fmask4.6 utilizes Landsat's TOA reflectance, brightness temperature data and other auxiliary data such as Global Surface Water Occurrence, DEM, etc. to identify clouds and cloud shadows based on the physical characteristics of clouds and incorporating probabilistic models. Fmask4.6 computes a Spectral-Contextual Snow Index (SCSI) by integrating the local SD of green band and NDSI to distinguish snow from clouds simply.

$$\text{NDSI} = (B_{\text{Green}} - B_{\text{SWIR}}) / (B_{\text{Green}} + B_{\text{SWIR}}) \quad (1)$$

$$\text{SCSI}_n = SD_n(B_{\text{Green}}) \times (1 - \text{NDSI}) \quad (2)$$

where, B is the TOA reflectance of green or SWIR band; n is the local window size in kilometers.

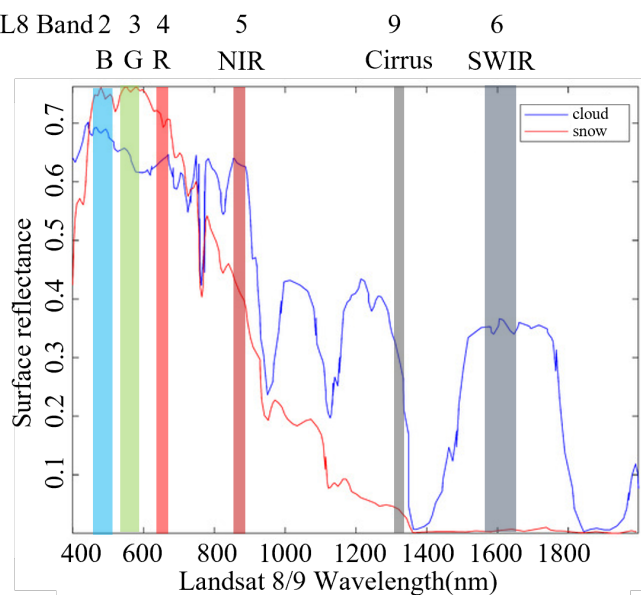


Fig. 2. Reflectance of clouds and snow and Landsat 8/9 bands.

A pixel is classified as snow/ice if its $SCSI_{10}$ is less than 0.0009 [34]. The cloud detection result is referred to as $Fmask$. $Fmask$ can extract most cloud pixels and distinguish part of snow from cloud. To further refine the cloud detection results and eliminate snow misclassified as clouds, a secondary cloud detection based on texture features will be employed.

B. Secondary Cloud Detection Based on Texture Features

Gray level co-occurrence matrices (GLCM) have been proved to be a very powerful texture descriptor used in image analysis [46]. Cloud cover typically exhibit irregular and soft textural features with significant grayscale and spatial variations, whereas snow cover generally displays more uniform textural details with smoother grayscale changes. The secondary procedure of proposed cloud detection algorithm relies on those textural features extracted from GLCM.

First, the entire remote sensing image is divided into equally spaced blocks (32×32 in this paper) which achieves an optimal balance between computational efficiency and accuracy metrics. Other parameter settings are discussed in Section V, with marginal regions smaller than a block size being treated as separate blocks. For each image block, the GLCM is computed, and textural features are derived from the GLCM. There are 14 statistical metrics derived from the GLCM: energy, entropy, contrast, homogeneity, correlation, etc.. And the most commonly used features are energy, contrast, correlation, homogeneity and entropy. P-values are calculated using the Mann-Whitney U test, and AUC values are derived from the receiver operating characteristic (ROC) curve. The features with p-values less than 0.01 and AUC scores exceeding 0.85 were selected (Energy and Correlation, as shown in Table II), which collectively validate their capacity in distinguishing clouds from cryospheric snow cover. The correlation and

Table II: Statistical Analysis of Features

Feature	p-Value	AUC
Correlation	5.8×10^{-4}	0.99
Energy	2.4×10^{-3}	0.92
Entropy	2.6×10^{-2}	0.85
Contrast	1.7×10^{-1}	0.64
Homogeneity	4.5×10^{-1}	0.63

energy features are named $Corr$ and $Engy$ and defined as follows:

$$Engy = \sum_i \sum_j p(i,j)^2 \quad (3)$$

$$Corr = \frac{\sum_i \sum_j (i - \mu_i)(j - \mu_j)p(i,j)}{\sigma_i \sigma_j} \quad (4)$$

In this study, 30 Regions of Interest (ROIs) were selected, with 15 representing snow and the remaining 15 representing clouds. The selection of ROIs followed a series of criteria to ensure the representativeness of various samples of the study. The ROIs were chosen to have a size similar to the blockSize, with rectangular shapes and uniform spatial distribution to represent various parts of the remote sensing image. Additionally, different types of clouds (e.g., tenuous clouds, thick clouds, discrete clouds, and continuous clouds) were considered. As shown in Fig.2, there were differences between clouds and snow in the shortwave infrared band; therefore, the B6 band($1.57\text{-}1.65\text{ }\mu\text{m}$) was selected for texture feature calculation and subsequent statistical analysis.

As shown in Fig.4, there are distinct differences in texture features between clouds and snow in terms of energy and correlation. To further distinguish between clouds and snow, thresholds can be set to eliminate snow components from potential cloud pixels. Specifically, the correlation threshold, $Corr_{th}$, is set within the range of [0.7, 0.9]; the energy threshold, $Engy_{th}$, is set within the range of [0.15, 0.4]; the texture detection result is called $Texture_{nor}$. The criteria for extracting clouds based on texture features is given by the following formula:

$$Texture = Corr > Corr_{th} \cap Engy < Engy_{th} \quad (5)$$

C. Cirrus Cloud Detection and Post processing

Cirrus clouds are primarily composed of ice crystals, and their spectral and textural properties closely resemble those of snow, which can lead to misclassification. Therefore, we need to perform separate detection for cirrus clouds when there are a significant number of cirrus clouds in the image. The proposed algorithm leverages the cirrus band(B9, $1.36\text{-}1.38\text{ }\mu\text{m}$) as an auxiliary data for cloud detection. By combining the spectral and textural characteristics of cirrus clouds, a more accurate identification of cirrus clouds can be achieved.

Using the correlation texture features in B6 and the spectral features in B9 can both effectively detect cirrus clouds, thereby improving the accuracy of the overall cloud detection results. In the following context, cloud detection results using the

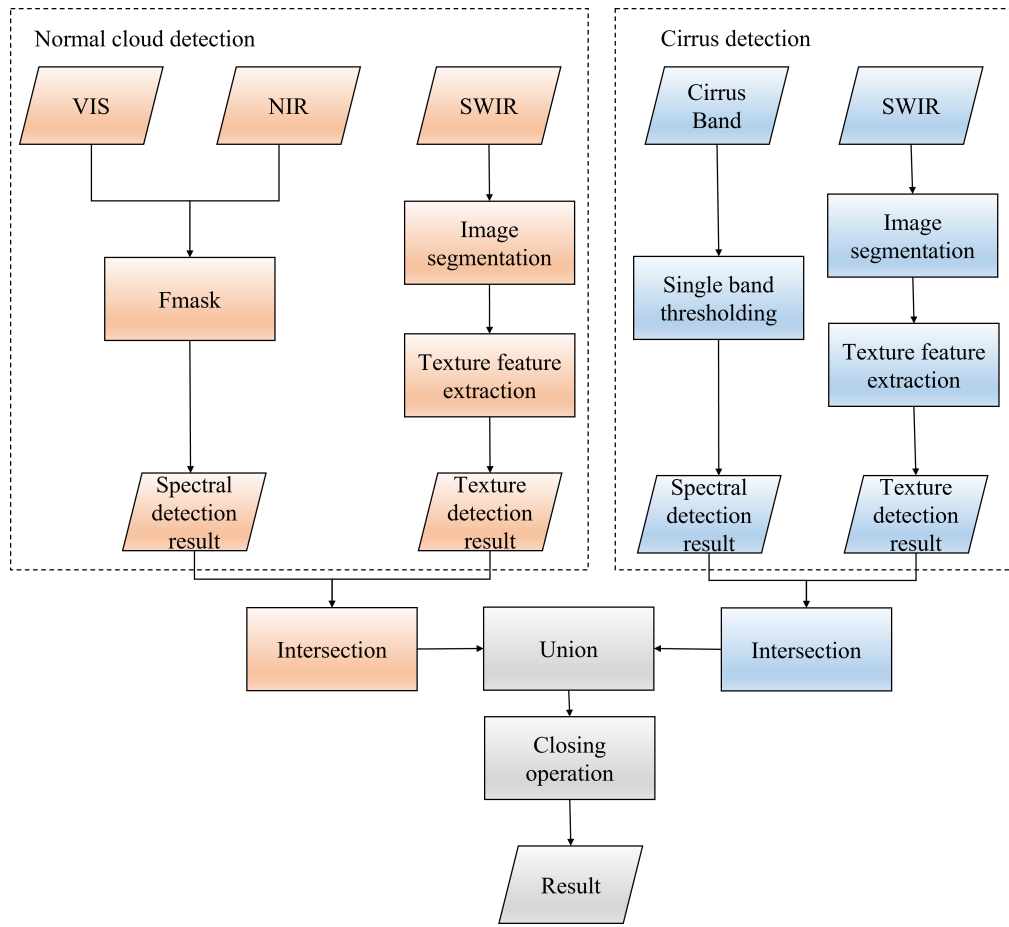


Fig. 3. Workflow of proposed cloud detection algorithm in polar regions.

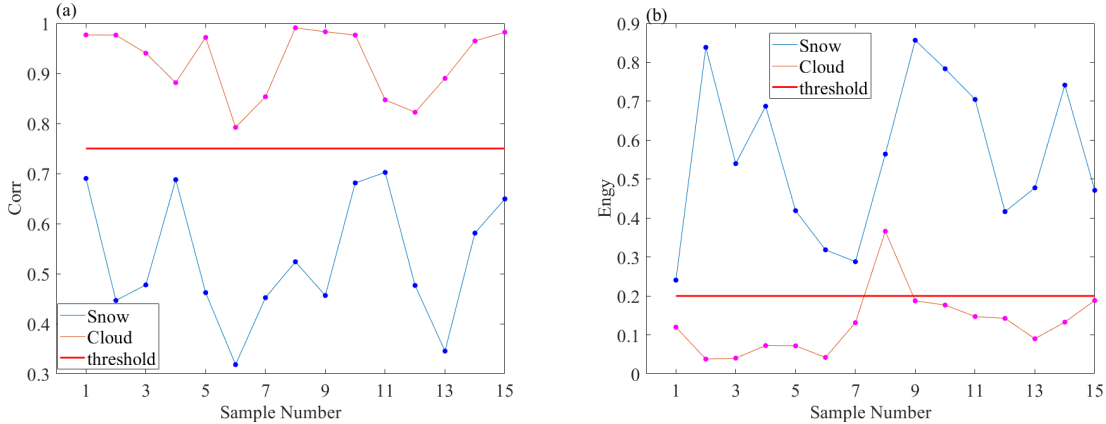


Fig. 4. Statistical analysis of Corr and Engy texture features for normal clouds and snow. (a) *Corr* texture features for normal clouds and snow, (b) *Engy* texture features for clouds and snow.

B6 band for cirrus texture characteristics are referred to as $Texture_{cir}(B6)$ with a correlation threshold set at 0.8, and results using the B9 band for cirrus spectral characteristics are referred to as $R_{cir}(B9)$ with a reflectance threshold set at 0.003. Although some snow blocks exhibit B9 reflectance greater than 0.003, a comprehensive analysis of spectral and textural features in Fig. 5 suggests that these two thresholds

can effectively extract most cirrus clouds while minimizing misclassification of snow. The final cloud masking procedure is implemented in two sequential steps: First, the intersection between the spectrum based cloud detection results and texture based results outcomes was calculated, including normal cloud and cirrus. Then the union of these two intersected results was computed to generate the final cloud mask product.

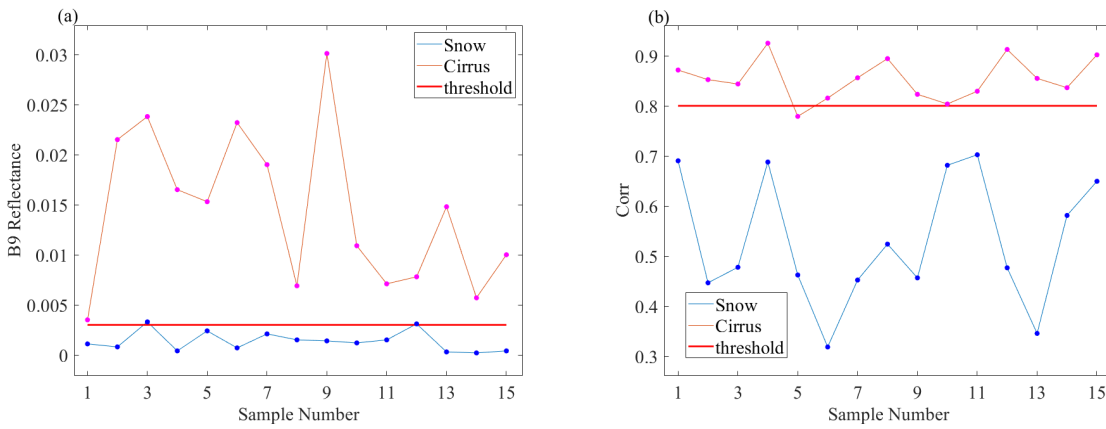


Fig. 5. Statistical analysis of spectral feature and $Corr$ for cirrus and snow. (a) B9 reflectance for cirrus and snow, (b) $Corr$ texture features for cirrus and snow.

The cloud detection formula incorporating the cirrus band is as follows:

$$\begin{aligned} Cloud = & (Texture_{cir}(B6) \cap R_{cir}(B9)) \\ & \cup (Texture_{nor}(B6) \cap Fmask) \end{aligned} \quad (6)$$

where, $Texture_{cir}(B6)$ is the cirrus cloud detection result based on texture features, $R_{cir}(B9)$ is the cirrus cloud detection result based on reflectance. $Texture_{cir}(B6)$ is the normal cloud detection result based on texture. $Fmask$ is the initial cloud detection result from Fmask. The final cloud mask is denoted as $Cloud$.

After cloud detection, there may be some small gaps or holes between clouds. To further refine the cloud detection results and fill potential gaps, morphological closing operations can be applied. The size of the window depends on the blocksize set before; here, we employ a window dimension of $2 \times$ blocksize for the closing operation.

D. Evaluation Metrics

In this study, the evaluation metrics is structured into two key components to assess the performance of the algorithm. Firstly, manually selected ROIs are served as true values and are compared with the algorithm's detection output. Secondly, the Landsat 8 Cloud Cover Assessment Validation Data, with cloud true values verified by remote sensing experts, is utilized for evaluation and compared with other existing algorithms. Precision, recall, overall accuracy and F-score are calculated to evaluate the performance of the algorithm. The creation of ROIs adheres to the following criteria: (1) Ambiguous cloud-snow mixed pixels, in addition to clearly identifiable clouds, are also classified as clouds because omission can have a greater impact on other remote sensing investigations; (2) The ROI spatial distribution is uniform and random; (3) ROIs should represent various types of clouds.

The formulas for accuracy, recall, precision and F-score are given by equations 7 to 10:

$$Accuracy = \frac{TP + TN}{TP + TN + FP + FN} \quad (7)$$

$$Recall = \frac{TP}{TP + FN} \quad (8)$$

$$Precision = \frac{TP}{TP + FP} \quad (9)$$

$$F-score = \frac{2 \times Precision \times Recall}{Precision + Recall} \quad (10)$$

where TP represents true positive, TN represents true negative, FP represents false positive, and FN represents false negative.

IV. RESULTS

In the following text, "original" refers to the original satellite imagery, "results" indicates the cloud detection outcomes from the algorithm proposed in section III, and "Fmask" denotes the cloud detection results obtained using the Fmask4.6. The results are divided into two parts: the first part focuses on the algorithm's robustness in various scenarios and improvement compared to Fmask4.6, while the second part evaluates the algorithm using the Landsat 8 Cloud Cover Assessment Validation Data. All algorithms were implemented using MATLAB version R2024b on AMD Ryzen 7 7800X3D 8-Core Processor and NVIDIA GeForce RTX 4060Ti GPU with 32-GB memory.

A. Performance Evaluation of the proposed algorithm

This study selected eight sets of remote sensing images to evaluate the algorithm's performance and improvements compared to Fmask4.6. These images include seven from Antarctica (Fig.6 (a1)-(g1)), representing the Antarctic thick-cloud areas, and tenuous cloud areas, one from Greenland, focusing on the coastal regions, as well as four from Tibetan Plateau and Tianshan Mountains to evaluate the algorithm's performances of mountains covered with snow. The choice of multiple coastal areas is twofold: firstly, the distinct texture changes at the land-sea boundary can lead to misclassification; secondly, it helps assess whether the algorithm mistakenly identifies sea ice as cloud.

Fmask4.6 demonstrated robust cloud-snow discrimination capabilities in heterogeneous scenes containing water bodies and multi-type clouds, achieving an average accuracy of 96% (Fig.6(f2, g2, h2)). However, its performance significantly degraded in spectrally ambiguous snow-cloud scenarios (Fig.6 (a2-d2)), where pronounced commission errors (snow misclassified as clouds) reduced precision: the precision of Fig.6 (a2,b2) were only 23.2% and 25.2% in Table III. In mountains regions (Fig.6(i2,j2,l2)), Fmask still shows misclassification of snow and cloud, resulting in high recall (99.8% averaged) but relatively low precision (68.6% averaged). Notably, Fig.6 (e2) revealed critical omission errors, with cloud detection recall plummeting to 2.9%, underscoring the algorithm's limited adaptability to environments dominated by spectrally overlapping snow and cloud features.

The proposed algorithm, enhanced by GLCM texture detection, addresses these shortcomings while preserving Fmask4.6's strengths. For scenarios where Fmask4.6 performed robustly (Fig.6 (f-h,k)), the method maintains equivalent accuracy. Crucially, in challenging cases (Fig.6 (a-e,i,j,l)). The algorithm's results elevate the overall average accuracy to 97.2%, demonstrating superior adaptability to common polar environments. The algorithm's precision rates are also significantly improved, with precision rates exceeding 97.8% in most scenarios. Although minor omissions of small-scale tenuous clouds occur in mountainous terrain (Fig.6 (l)), the proposed algorithm maintains superior detection accuracy with an average F1-score of 91.6% across test scenarios. The results indicate that the proposed algorithm enhance the ability to distinguish between snow/sea ice and clouds.

In addition to the prominent features commonly found in remote sensing images, such as thick clouds and extensive cirrus clouds, the detection of discrete tenuous clouds has long been a challenge in the field of cloud detection [47]. Due to their discrete distribution in images, these tenuous clouds are often difficult to detect and identify accurately for traditional algorithms. As shown in Fig.7, our algorithm successfully detected the discretely distributed tenuous clouds within the red box area, demonstrating the performance in tenuous cloud detection.

B. Comparison with existing algorithms

This study utilized the "Landsat 8 Cloud Cover Assessment Validation Data" (L8 Biome) which was verified by remote sensing experts for accuracy assessment [44], [45]. Previous work by Foga et al. compared various cloud detection algorithms using this dataset, revealing that the cloud detection accuracy in most ice and snow scenes ranged from 60% to 70% [45]. This research selected three ice and snow scene images for cloud detection: two from Antarctica and one from Greenland. In the L8 Biome dataset, clouds are categorized as "tenuous clouds" and "thick clouds." This study combined these into a single "cloud" category, merging other categories into "non-cloud" for accuracy evaluation. As shown in Fig.8 and Table.IV, the cloud detection results from this algorithm exhibit high consistency with those of the L8 Biome dataset; the accuracy of the proposed algorithm exceeds 90%. The

recall rate for Fig.8(a) is relatively low, while Fig.8(c) has a slightly lower precision rate. This may be due to the L8 Biome dataset's incomplete classification of clouds, which is a problem we would thoroughly discuss in section V. Nevertheless, the proposed algorithm demonstrates excellent performance, with an average precision rate and average accuracy rate both above 90%. Some misclassifications or omissions relate to the ambiguity of the cloud definition; for instance, the tenuous clouds in the middle area of Fig.8 (c) were classified as non-clouds in the L8 Biome dataset, whereas the proposed algorithm detected them as clouds.

Table V compares the evaluation metrics between our approach and other widely used cloud detection algorithms, namely Cfmask [33], ACCA [14] and their different variations cfmask-t-cirrus (utilizing thermal infrared and cirrus bands), cfmask-nt-cirrus (excluding thermal infrared), and AT-ACCA (employing artificial thermal infrared bands). CloudFCN [25] and RS-Net [26] are two widely recognized deep learning algorithms for cloud detection tasks. Most of them exhibit high recall rates but lower precision rates because of misclassification of snow and cloud, leading to lower omission errors and higher commission errors. For example, the cfmask-nt-cirrus algorithm, faces above issues since snow and clouds have similar characteristics in the visible spectrum, resulting in significant snow being misclassified as cloud. Consequently, its precision is only 36.5%, with a corresponding misclassification rate of 63.5%. The F-score of 0.53 reflects a relatively poor performance in ice and snow environments.

In summary, the proposed algorithm demonstrates excellent performance in terms of recall rate, precision rate, and accuracy, particularly surpassing most of the comparative algorithms in precision and accuracy. The F-score of this algorithm is 0.91, excellently higher than that of other algorithms, indicating a well-balanced recall rate and precision rate. Other algorithms, such as cfmask and ACCA, although having high recall rates, exhibit low precision rates, resulting in lower F-scores. This suggests that these algorithms tend to misclassify non-cloud pixels (such as snow) as cloud.

V. DISCUSSION

A review of the L8 Biome dataset used for accuracy assessment revealed several contentious classifications of ambiguous pixels, which may impact the reliability of the algorithm's accuracy data [45]. It is noteworthy that the standard definitions of clouds can also affect algorithm performance. The thickness of clouds can also influence detection—should very tenuous clouds be classified as clouds? Furthermore, are there clear classification criteria for some ambiguous pixels? For instance, in the red box area of Fig.9, The area covered by tenuous cloud is not masked by L8 Biome, whereas our algorithm successfully detected the presence of tenuous clouds although the bedrock can be fuzzily recognized through translucent thin clouds. This difference of classification results is likely due to the ambiguous nature of the tenuous cloud pixels, which leads to their exclusion as cloud pixels in the manual masking process. Addressing these issues will facilitate future accuracy assessments and algorithm comparisons.

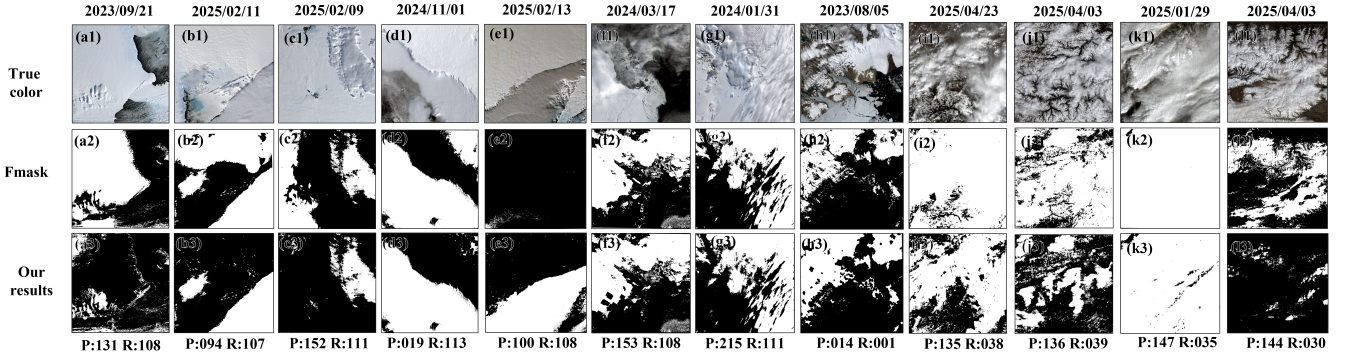


Fig. 6. Results of cloud detection (a1)-(l1) True color with (B4, B3, B2). (a2)-(l2) Fmask cloud detection results. (a3)-(l3) Our cloud detection results.

Table III: Comparison of Fmask and Our Results

Fig.6 Number	Fmask			Our Results		
	Recall	Precision	Accuracy	Recall	Precision	Accuracy
a	81.10%	23.20%	26.00%	80.4%	96.8%	96.0%
b	99.5%	25.2%	47.9%	99.5%	99.5%	99.4%
c	97.6%	73.4%	76.9%	97.6%	99.9%	99.6%
d	100.0%	77.6%	89.7%	100.0%	98.9%	99.5%
e	2.9%	100.0%	68.8%	100.0%	99.3%	99.5%
f	95.9%	93.8%	95.0%	95.6%	97.4%	96.3%
g	91.9%	99.9%	94.4%	91.9%	99.9%	94.4%
h	96.9%	99.8%	98.6%	97.4%	99.3%	98.8%
i	99.9%	66.0%	98.3%	97.8%	97.7%	97.8%
j	99.8%	61.4%	83.1%	85.2%	95.7%	89.7%
k	100%	85.8%	99.4%	99.7%	90.2%	99.6%
l	99.6%	61.4%	63.2%	53.9%	98.4%	96.2%
Average	88.7%	72.3%	78.4%	91.6%	97.8%	97.2%

Table IV: Accuracy Assessment based on L8 Biome Images

Fig.8 Number	Recall	Precision	Accuracy
(a)	69.0%	95.0%	90.7%
(b)	97.1%	98.7%	97.9%
(c)	97.9%	88.8%	91.3%
Average	88.0%	94.2%	93.3%

Table V: Accuracy Comparison of Various Cloud Detection Algorithms in Ice and Snow Environments

Fig.8 Name	Recall	Precision	Accuracy	F-score
cfmask	86.6%	75.7%	64.1%	0.81
cfmask-t-cirrus	94.3%	36.5%	45.1%	0.53
cfmask-nt-cirrus	99.2%	36.5%	48.4%	0.53
ACCA	99.3%	71.6%	67.9%	0.83
AT-ACCA	98.4%	69.5%	68.3%	0.81
CloudFCN	82.4%	72.5%	72.9%	0.77
RS-Net	84.5%	50.1%	62.9%	0.63
Our results	88.0%	94.2%	93.3%	0.91

In polar regions, there are other cloud-related targets that are worth extracting, such as cloud shadows and blowing snow. The Fmask algorithm has demonstrated good performance in detecting cloud shadows [8]. The focus of this work is to enhance the algorithm's capability for cloud extraction in polar ice and snow environments, and thus, a separate module

on cloud shadow detection is not included, but the cloud shadow detection efficacy of Fmask can still be integrated into the algorithm presented in this paper, thereby broadening its applicability. The uplift and horizontal transport of snow by wind, heretofore referred to as blowing snow, occurs frequently in polar regions [48]. The presence of blowing snow is a concern for remote sensing of surface and atmospheric factors and exhibits similar spectral and textural characteristics to clouds [49], which may lead to misclassification [50]. The blowing snow was not observed in our experiment. Other targets such as rocks, which are misclassified as clouds in Fig.6 (d3). However, the area covered by rocks is relatively small, accounting for less than 0.2% in Antarctica [51]. Moreover, the exposed rocks are stationary, and their identification can be further refined using the existing dataset of exposed rocks.

Furthermore, the algorithm introduced in this paper does not involve any specialized processing of thermal infrared data. Because Fmask employs a threshold method based on brightness temperature to assist in cloud detection [8], but this approach may not yield optimal results in polar regions where both clouds and snow exhibit low temperatures. This observation is consistent with the findings in Section IV-B, where the cfmask-nt-cirrus algorithm, which operates without thermal infrared data, demonstrates higher accuracy compared to the cfmask-t-cirrus algorithm, which incorporates thermal infrared data [45]. Another noteworthy point is that not all

Table VI: Performance Metrics for Different Block Sizes and Thresholds

Fig.10 Number	blocksize	$Corr_{th}$	$Engy_{th}$	B_{cirrus} reflectance	$CircusCorr_{th}$	Times/s	Recall	Precision	Accuracy
(b)	32	0.85	0.3	0.003	0.8	2486	80.4%	96.8%	96.0%
(c)	64	0.85	0.3	0.003	0.8	838	80.4%	96.4%	95.5%
(d)	128	0.85	0.3	0.003	0.8	280	71.0%	94.4%	93.2%
(e)	32	0.7	0.4	0.003	0.8	3654	80.6%	78.7%	78.8%
(f)	32	0.9	0.15	0.003	0.8	2022	79.2%	96.9%	96.0%
(g)	\	\	\	\	\	49	81.1%	23.2%	26.0%

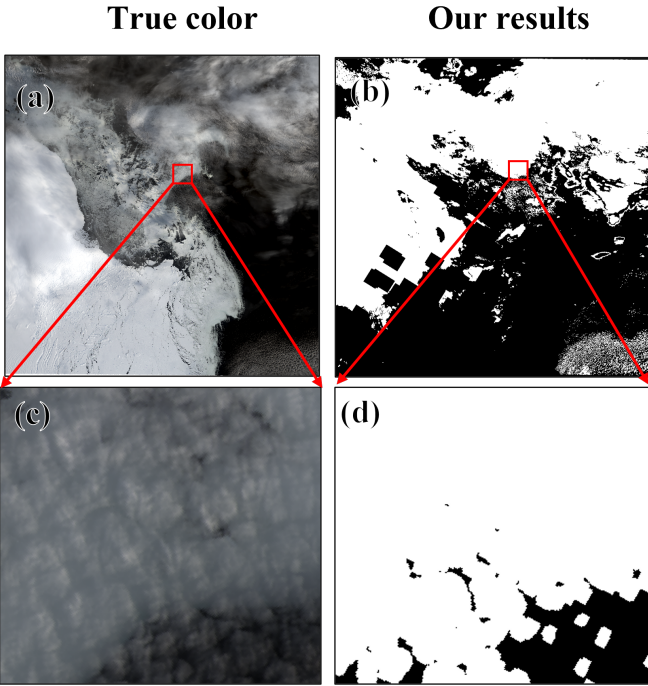


Fig. 7. The details of tenuous cloud detection. (a) the true color Landsat image, (b) cloud detection results from our algorithm, (c) and (d) highlight the details of (a) and (b).

snow and ice scenes result in poor performance by Fmask; indeed, even in polar regions, Fmask can identify clouds in some instances. However, compared to other regions, Fmask generally exhibits lower performance in polar areas.

Some cloud detection algorithms developed for polar regions may produce poor results when applied to other snow/ice environment such as Northern Europe, Siberia [30]. However, our algorithm is expected to yield favorable results. Given that Fmask has demonstrated robust performance in these areas, it's likely that even in non-polar regions, where texture features might misclassify rough surfaces as clouds, these errors will be corrected due to significant spectral differences from real clouds. Consequently, our algorithm has the potential to be generalized for use in other snow and ice-covered landscapes out of polar regions.

Currently, processing a single Landsat 8 image takes between 0.3 and 2 hours while Fmask takes only 1-10 minutes, depending on parameter settings and cloud coverage. This algorithm's computational efficiency could be further enhanced. Users can select appropriate sub-block sizes according to their specific needs, trading-off improvements between detection

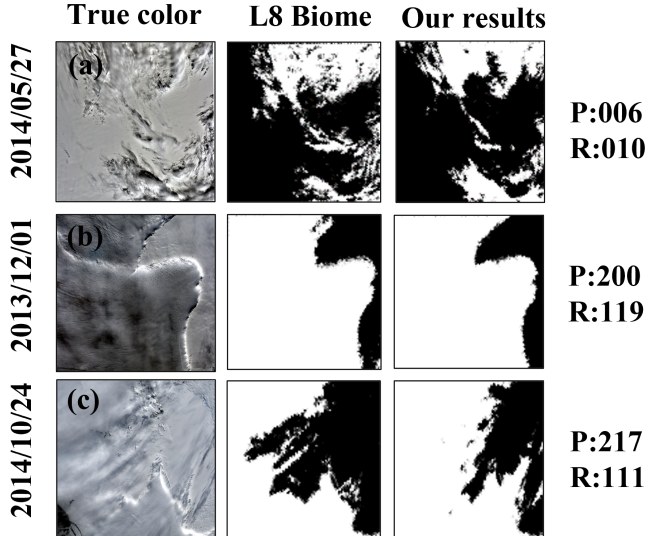


Fig. 8. Comparison of L8 Biome and Detection Results. (a) inland Greenland, (b) thick cloud in Antarctic inland, (c) thick and tenuous clouds coexisting in Antarctic inland

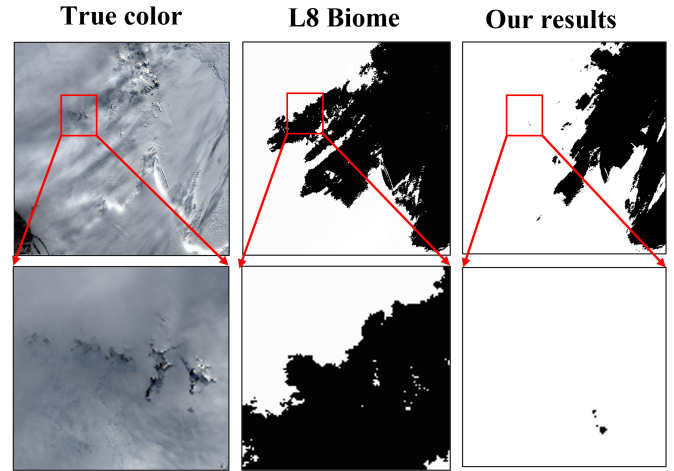


Fig. 9. The red box highlights the details of the cloud detection results of our algorithm and L8 biome

accuracy and computational efficiency. The default value of the block is 32, with a runtime of approximately 1 hour. Increasing the block value can speed up the running time, but an excessively large block size may affect the performance of the algorithm, as shown in Fig.10 (d) and Table VI. A promising approach to enhance the algorithm's utility in op-



Fig. 10. Parameter sensitivity analysis. (a) True color, (b) blocksize=32, $Corr_{th}=0.85$, $Engy_{th} = 0.3$, (c) blocksize=64, $Corr_{th} = 0.85$, $Engy_{th} = 0.3$, (d) blocksize=128, $Corr_{th} = 0.85$, $Engy_{th} = 0.3$, (e) blocksize=32, $Corr_{th} = 0.7$, $Engy_{th} = 0.4$, (f) blocksize=32, $Corr_{th} = 0.9$, $Engy_{th} = 0.15$, (g) Fmask.

erational scenarios is to translate it from MATLAB to a more computationally efficient language such as C. For example, Zhu Z has successfully transferred the Fmask algorithm to C, creating the cfmask algorithm [8], reducing the computational time to a mere 10% of the original, unlocking the potential for large-scale, high-throughput processing. By transferring our algorithm to C, the processing time for a single image can be confined to within a few minutes, thereby enhancing the algorithm's viability for operational deployment.

Thresholds also impact the accuracy of the algorithm. As shown in Fig.10, coastal pixels are misclassified as cloud due to abrupt textural variations along coastlines. However, this phenomenon does not consistently occur, as demonstrated by the accurate coastal delineation observed in Figs.6 (f) and (h). Reducing the blocksize parameter can effectively diminish such errors. Furthermore, parameter sensitivity tests indicate that lower $Corr_{th}$ combined with higher $Engy_{th}$ may lead to increased misclassification (Fig.10 (e)). Therefore, the setting of the threshold should be based on the proportion of cloud in the imagery. When the imagery contains a small proportion of cloud, strict parameter settings can be applied; conversely, when there is a higher proportion of cloud, less strict settings should be used.

This algorithm can be extended to other multispectral sensors such as FY-3D MERSI by establishing inter-sensor band correspondences based on radiative equivalence. By aligning homologous spectral bands (e.g., visible, shortwave infrared) while accounting for spectral response function differences, it enables multi-source satellite synergies for improved cloud monitoring. Future work should develop standardized spectral translation protocols addressing inter-sensor variations in spectral resolution and bandpass characteristics, along with adaptive calibration frameworks to compensate for spectral response discrepancies [52].

VI. CONCLUSION

Cloud cover is a common issue in optical remote sensing satellite imagery, which can obscure land surface information retrieval and reduce the accuracy of data analysis. This study addresses the issue of cloud detection in polar ice and snow environments, by proposing a novel cloud detection algorithm. This algorithm combines spectral and texture characteristics to enhance the ability to distinguish between clouds and snow, thereby improving cloud detection performances in polar regions. The algorithm presented in this study achieves an average recall rate of 88%, an average precision rate of 94%,

an average overall accuracy of 93%, and an F-score of 0.91 on Landsat 8 Cloud Cover Assessment Validation Data in polar regions, representing an average accuracy improvement of 60% and an average F-score improvement of 30% compared to Fmask, ACCA and other conventional algorithms, while also eliminating the need for pre-training in machine or deep learning, reducing the costs of labeling.

In summary, this study integrates the ideas from various previous methods to propose a new cloud detection technique for optical remote sensing imagery in ice and snow environments. This method generates cloud masks and performs well in most polar ice/snow scenarios, and demonstrating its potential for broader application to other sensors and integration into operational cloud processing workflows.

VII. ACKNOWLEDGMENT

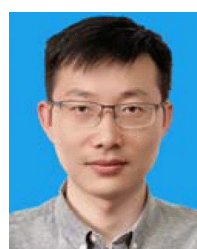
The authors would like to thank NASA and USGS for providing the Landsat data, as well as the developers of the “Landsat 8 Cloud Cover Assessment Validation Data” and the Fmask algorithm for their open-source contributions. All the codes used in this study are available at <https://github.com/Versatilecos/PolarCloudDetection>.

REFERENCES

- [1] S. Sandven and O. M. Johannessen, *Sea ice monitoring by remote sensing*. The American Society for Photogrammetry & Remote Sensing, 2006, ch. 8.
- [2] T. Li, M. Shokr, Y. Liu, X. Cheng, T. Li, F. Wang, and F. Hui, “Monitoring the tabular icebergs C28A and C28B calved from the Mertz Ice Tongue using radar remote sensing data,” *Remote Sensing of Environment*, vol. 216, pp. 615–625, 2018.
- [3] T. Li, Y. Liu, T. Li, F. Hui, Z. Chen, and X. Cheng, “Antarctic surface ice velocity retrieval from MODIS-based mosaic of Antarctica (MOA),” *Remote Sensing*, vol. 10, no. 7, p. 1045, 2018.
- [4] R. Massom and D. Lubin, *Polar remote sensing*. Springer, 2006, vol. 2.
- [5] Y. Li, W. Chen, Y. Zhang, C. Tao, R. Xiao, and Y. Tan, “Accurate cloud detection in high-resolution remote sensing imagery by weakly supervised deep learning,” *Remote Sensing of Environment*, vol. 250, p. 112045, 2020.
- [6] Y. Zhang, W. B. Rossow, A. A. Lacis, V. Oinas, and M. I. Mishchenko, “Calculation of radiative fluxes from the surface to top of atmosphere based on ISCCP and other global data sets: Refinements of the radiative transfer model and the input data,” *Journal of Geophysical Research: Atmospheres*, vol. 109, no. D19, p. D19105, 2004.
- [7] X. Zhu and E. H. Helmer, “An automatic method for screening clouds and cloud shadows in optical satellite image time series in cloudy regions,” *Remote sensing of environment*, vol. 214, pp. 135–153, 2018.
- [8] Z. Zhu and C. E. Woodcock, “Object-based cloud and cloud shadow detection in Landsat imagery,” *Remote sensing of environment*, vol. 118, pp. 83–94, 2012.

- [9] S. Qiu, B. He, Z. Zhu, Z. Liao, and X. Quan, "Improving Fmask cloud and cloud shadow detection in mountainous area for Landsats 4–8 images," *Remote Sensing of Environment*, vol. 199, pp. 107–119, 2017.
- [10] Z. Zhu and C. E. Woodcock, "Automated cloud, cloud shadow, and snow detection in multitemporal Landsat data: An algorithm designed specifically for monitoring land cover change," *Remote Sensing of Environment*, vol. 152, pp. 217–234, 2014.
- [11] L. Feng and X. Wang, "Quantifying cloud-free observations from landsat missions: implications for water environment analysis," *Journal of Remote Sensing*, vol. 4, p. 0110, 2024.
- [12] T. Lachlan-Cope, "Antarctic clouds," *Polar Research*, vol. 29, no. 2, pp. 150–158, 2010.
- [13] Z. Liu and Y. Wu, "A review of cloud detection methods in remote sensing images," *Remote Sens. Land Resour*, vol. 29, no. 4, pp. 6–7, 2017.
- [14] R. R. Irish, J. L. Barker, S. N. Goward, and T. Arvidson, "Characterization of the Landsat-7 ETM+ Automated Cloud-Cover Assessment (ACCA) algorithm," *Photogrammetric Engineering & Remote Sensing*, vol. 72, no. 10, pp. 1179–1188, 2006.
- [15] Z. Li, H. Shen, Q. Weng, Y. Zhang, P. Dou, and L. Zhang, "Cloud and cloud shadow detection for optical satellite imagery: Features, algorithms, validation, and prospects," *ISPRS Journal of Photogrammetry and Remote Sensing*, vol. 188, pp. 89–108, 2022.
- [16] Y. Sui, B. He, and T. Fu, "Energy-based cloud detection in multispectral images based on the SVM technique," *International Journal of Remote Sensing*, vol. 40, no. 14, pp. 5530–5543, 2019.
- [17] G. Chen and D. E., "Support vector machines for cloud detection over ice-snow areas," *Geo-spatial Information Science*, vol. 10, no. 2, pp. 117–120, 2007.
- [18] X. Kang, G. Gao, Q. Hao, and S. Li, "A coarse-to-fine method for cloud detection in remote sensing images," *IEEE Geoscience and Remote Sensing Letters*, vol. 16, no. 1, pp. 110–114, 2019.
- [19] M. T. Amare, S. T. Demissie, S. A. Beza, and S. H. Errena, "Impacts of land use/land cover changes on the hydrology of the fafan catchment ethiopia," *Journal of Geovisualization and Spatial Analysis*, vol. 8, no. 1, p. 10, 2024.
- [20] J. Wei, W. Huang, Z. Li, L. Sun, X. Zhu, Q. Yuan, L. Liu, and M. Cribb, "Cloud detection for landsat imagery by combining the random forest and superpixels extracted via energy-driven sampling segmentation approaches," *Remote Sensing of Environment*, vol. 248, p. 112005, 2020.
- [21] P. Li, L. Dong, H. Xiao, and M. Xu, "A cloud image detection method based on SVM vector machine," *Neurocomputing*, vol. 169, pp. 34–42, 2015.
- [22] S. Mahajan and B. Fataniya, "Cloud detection methodologies: variants and development—a review," *Complex & Intelligent Systems*, vol. 6, no. 2, pp. 251–261, 2019.
- [23] P. Dou, H. Shen, C. Huang, Z. Li, Y. Mao, and X. Li, "Large-scale land use/land cover extraction from landsat imagery using feature relationships matrix based deep-shallow learning," *International Journal of Applied Earth Observation and Geoinformation*, vol. 129, p. 103866, 2024.
- [24] F. Xie, M. Shi, Z. Shi, J. Yin, and D. Zhao, "Multilevel cloud detection in remote sensing images based on deep learning," *IEEE Journal of Selected Topics in Applied Earth Observations and Remote Sensing*, vol. 10, no. 8, pp. 3631–3640, 2017.
- [25] A. Francis, P. Sidiropoulos, and J.-P. Muller, "CloudFCN: Accurate and robust cloud detection for satellite imagery with deep learning," *Remote Sensing*, vol. 11, no. 19, p. 2312, 2019.
- [26] J. H. Jeppesen, R. H. Jacobsen, F. Inceoglu, and T. S. Toftegaard, "A cloud detection algorithm for satellite imagery based on deep learning," *Remote sensing of environment*, vol. 229, pp. 247–259, 2019.
- [27] J. Guo, J. Yang, H. Yue, H. Tan, C. Hou, and K. Li, "CDNetV2: CNN-based cloud detection for remote sensing imagery with cloud-snow coexistence," *IEEE Transactions on Geoscience and Remote Sensing*, vol. 59, no. 1, pp. 700–713, 2021.
- [28] J. Li and Q. Wang, "CSDFormer: A cloud and shadow detection method for landsat images based on transformer," *International Journal of Applied Earth Observation and Geoinformation*, vol. 129, p. 103799, 2024.
- [29] J. Yang, W. Li, K. Chen, Z. Liu, Z. Shi, and Z. Zou, "Weakly supervised adversarial training for remote sensing image cloud and snow detection," *IEEE Journal of Selected Topics in Applied Earth Observations and Remote Sensing*, 2024.
- [30] C. Poulsen, U. Egede, D. Robbins, B. Sandeford, K. Tazi, and T. Zhu, "Evaluation and comparison of a machine learning cloud identification algorithm for the SLSTR in polar regions," *Remote Sensing of Environment*, vol. 248, p. 111999, 2020.
- [31] Y. Zhan, J. Wang, J. Shi, G. Cheng, L. Yao, and W. Sun, "Distinguishing cloud and snow in satellite images via deep convolutional network," *IEEE geoscience and remote sensing letters*, vol. 14, no. 10, pp. 1785–1789, 2017.
- [32] M. Xu, X. Jia, and M. Pickering, "Automatic cloud removal for Landsat 8 OLI images using cirrus band," in *2014 IEEE Geoscience and Remote Sensing Symposium*. IEEE, 2014, pp. 2511–2514.
- [33] Z. Zhu, S. Wang, and C. E. Woodcock, "Improvement and expansion of the Fmask algorithm: Cloud, cloud shadow, and snow detection for Landsats 4–7, 8, and Sentinel 2 images," *Remote sensing of Environment*, vol. 159, pp. 269–277, 2015.
- [34] S. Qiu, Z. Zhu, and B. He, "Fmask 4.0: Improved cloud and cloud shadow detection in Landsats 4–8 and Sentinel-2 imagery," *Remote Sensing of Environment*, vol. 231, p. 111205, 2019.
- [35] T. Wu and L. Han, "Cloud extraction scheme for multi-spectral images using Landsat-8 OLI images with high brightness reflectivity covered," *IEEE Access*, vol. 8, pp. 3387–3396, 2020.
- [36] S. Dong, C. Gong, Y. Hu, F. Zheng, and Z. He, "Polar cloud detection of FengYun-3d medium resolution spectral imager II imagery based on the radiative transfer model," *Remote Sensing*, vol. 15, no. 21, p. 5221, 2023.
- [37] D. H. Bromwich, J. P. Nicolas, K. M. Hines, J. E. Kay, E. L. Key, M. A. Lazzara, D. Lubin, G. M. McFarquhar, I. V. Gorodetskaya, D. P. Grosvenor *et al.*, "Tropospheric clouds in antarctica," *Reviews of Geophysics*, vol. 50, no. 1, p. RG1004, 2012.
- [38] C. Kittel, C. Amory, S. Hofer, C. Agosta, N. C. Jourdain, E. Gilbert, L. Le Toumelin, E. Vignon, H. Gallée, and X. Fettweis, "Clouds drive differences in future surface melt over the Antarctic ice shelves," *The Cryosphere*, vol. 16, no. 7, pp. 2655–2669, 2022.
- [39] J. T. M. Lenaerts, K. Van Tricht, S. Lhermitte, and T. S. L'Ecuyer, "Polar clouds and radiation in satellite observations, reanalyses, and climate models," *Geophysical Research Letters*, vol. 44, no. 7, pp. 3355–3364, 2017.
- [40] M. D. Shupe and J. M. Intrieri, "Cloud radiative forcing of the Arctic surface: The influence of cloud properties, surface albedo, and solar zenith angle," *Journal of climate*, vol. 17, no. 3, pp. 616–628, 2004.
- [41] A. Lacour, H. Chepfer, N. B. Miller, M. D. Shupe, V. Noel, X. Fettweis, H. Galée, J. E. Kay, R. Guzman, and J. Cole, "How well are clouds simulated over greenland in climate models? consequences for the surface cloud radiative effect over the ice sheet," *Journal of Climate*, vol. 31, no. 22, pp. 9293–9312, 2018.
- [42] J. D. Spinhirne, S. P. Palm, and W. D. Hart, "Antarctica cloud cover for October 2003 from GLAS satellite lidar profiling," *Geophysical Research Letters*, vol. 32, no. 22, 2005.
- [43] X. Liu, T. He, L. Sun, X. Xiao, S. Liang, and S. Li, "Analysis of daytime cloud fraction spatiotemporal variation over the Arctic from 2000 to 2019 from multiple satellite products," *Journal of Climate*, vol. 35, no. 23, pp. 7595–7623, 2022.
- [44] P. Scaramuzza, S. Foga, and J. Dwyer, "L8 biome cloud validation masks," 2016.
- [45] S. Foga, P. L. Scaramuzza, S. Guo, Z. Zhu, R. D. Dilley Jr, T. Beckmann, G. L. Schmidt, J. L. Dwyer, M. J. Hughes, and B. Laue, "Cloud detection algorithm comparison and validation for operational Landsat data products," *Remote sensing of environment*, vol. 194, pp. 379–390, 2017.
- [46] X. Huang, X. Liu, and L. Zhang, "A multichannel gray level co-occurrence matrix for multi/hyperspectral image texture representation," *remote sensing*, vol. 6, no. 9, pp. 8424–8445, 2014.
- [47] H. Shen, H. Li, Y. Qian, L. Zhang, and Q. Yuan, "An effective thin cloud removal procedure for visible remote sensing images," *ISPRS Journal of Photogrammetry and Remote Sensing*, vol. 96, pp. 224–235, 2014.
- [48] S. P. Palm, Y. Yang, J. D. Spinhirne, and A. Marshak, "Satellite remote sensing of blowing snow properties over antarctica," *Journal of Geophysical Research: Atmospheres*, vol. 116, no. D16, 2011.
- [49] T. A. Scambos, T. M. Haran, M. A. Fahnestock, T. H. Painter, and J. Bohlander, "MODIS-based Mosaic of Antarctica (MOA) data sets: Continent-wide surface morphology and snow grain size," *Remote sensing of environment*, vol. 111, no. 2, pp. 242–257, 2007.
- [50] U. Herzfeld, A. Hayes, S. Palm, D. Hancock, M. Vaughan, and K. Barbieri, "Detection and height measurement of tenuous clouds and blowing snow in icesat-2 atlas data," *Geophysical Research Letters*, vol. 48, no. 17, p. e2021GL093473, 2021.
- [51] A. Burton-Johnson, M. Black, P. T. Fretwell, and J. Kaluza-Gilbert, "An automated methodology for differentiating rock from snow, clouds and sea in antarctica from landsat 8 imagery: a new rock outcrop map

- and area estimation for the entire antarctic continent," *The Cryosphere*, vol. 10, no. 4, pp. 1665–1677, 2016.
- [52] M. Claverie, J. Ju, J. G. Masek, J. L. Dungan, E. F. Vermote, J.-C. Roger, S. V. Skakun, and C. Justice, "The harmonized landsat and sentinel-2 surface reflectance data set," *Remote sensing of environment*, vol. 219, pp. 145–161, 2018.



Lei Zheng received the Ph.D. degree in photogrammetry and remote sensing from Wuhan University, Wuhan, China, in 2019. He is currently an Associate Professor with Sun Yat-Sen University, Guangzhou, China. He has authored or coauthored about 20 publications in refereed journals. His research interests include remote sensing of snow and ice, snow/permafrost/river thermal model, snow microwave emission/backscatter model, with a focus on the melting processes and climate variability in the cryosphere.



Xinran Shen was born in Henan, China, in 2002. He received the Remote Sensing Science and Technology and Information and Computational Science B.E. degree from Sun Yat-Sen University, Guangdong Province, China. He is currently working toward his Ph.D. at the School of Geospatial Engineering and Science, Sun Yat-Sen University, Zhuhai, China. His current research interests include polar remote sensing, and glacier modeling.



Qi Liang received the B.S. degree in information and computing science from the Harbin Institute of Technology, Harbin, China, in 2010, and the M.S. and Ph.D. degrees in photogrammetry and remote sensing from Wuhan University, Wuhan, China, in 2014 and 2019, respectively. He is currently an Associate Professor with the School of Geospatial Engineering and Science, Sun Yat-sen University, Guangzhou, China. His research interests include using satellite data to monitor glacier changes in Antarctica and Greenland and understand its response to climate change.



Teng Li was born in Xuzhou, China. He received the B.Sc. degree in geographic science from Wuhan University, Wuhan, China, in 2015, and the Ph.D. degree in global environmental change from Beijing Normal University, Beijing, China, in 2021. He is currently an Assistant Professor with the School of Geospatial Engineering and Science, Sun Yat-Sen University, Zhuhai, China. His research interests include image processing, glacial dynamics, ice sheet mass balance, and UAV operation.



Xiao Cheng was born in Nanjing, China, in 1976. He received the B.E. and M.tech. degrees in engineering survey from the Wuhan Technical University of Surveying and Mapping, Wuhan, China, in 1998 and 2001, respectively, and the Ph.D. degree in cartography and geographical information system from the Graduate School of Chinese Academy of Social Sciences, Beijing, China, in 2004. In 2004, he joined the Institute of Remote Sensing Applications, Chinese Academy of Sciences, as an Assistant Researcher, and in 2008, became an Associate Researcher. In 2009, he moved to Beijing Normal University and serve as the Associate Dean of the College of Global Change and Earth System Science (GCESS), and became a Professor. In 2016, he became the Dean of GCESS. In 2019, he joined Sun Yat-Sen University, initiated the School of Geospatial Engineering and Science and act as the Dean. His current research interests include polar remote sensing technology and climate change in polar regions. He has authored or coauthored more than 100 peer-reviewed journal papers, including PNAS, RSE, and other top international geoscience journals. Dr. Cheng was a recipient of the Award for distinguished individual of China's polar exploration in 2017.



Chong Liu received the B.E. and Ph.D. degrees in photogrammetry and remote sensing from Wuhan University, Wuhan, China, in 2010 and 2015, respectively. He is currently an Associate Professor with the School of Geospatial Engineering and Science, Sun Yat-sen University, Guangzhou, China. His research interests include using satellite data to monitor glacier changes in Antarctica and Greenland and understand its response to climate change.



Jiaqi Yao received the B.Sc. degree in Surveying and Mapping Engineering from North China University of Science and Technology, Tangshan, China, in 2017, the M.Sc. degree in photogrammetry and remote sensing from Liaoning Technical University, in 2019, and the Ph.D. degree in photogrammetry and remote sensing from College of Geomatics, Shandong University of Science and Technology, Qingdao, China, in 2022. He is currently a associate professor with the Tianjin Normal University. His research interests include cloud detection, cloud-snow separation and aerosol optical depth inversion by machine learning in satellite remote sensing.



Shaoyin Wang received the M.S. degree from the Chinese Academy of Sciences, Beijing, China, in 2016, and the Ph.D. degree from the Karlsruhe Institute of Technology, Karlsruhe, Germany, in 2019. He is currently an Associate Professor with the School of Geospatial Engineering and Science, Sun Yat-Sen University, Zhuhai, China. His research interest is polar climate change with a focus on sea ice variability.